

# Microphysical and Geometrical Controls on the Pattern of Orographic Precipitation

GERARD H. ROE AND MARCIA B. BAKER

*Department of Earth and Space Sciences, University of Washington, Seattle, Washington*

(Manuscript received 25 May 2004, in final form 2 May 2005)

## ABSTRACT

Patterns of orographic precipitation can vary significantly both in time and space, and such variations must ultimately be related to mountain geometry, cloud microphysics, and synoptic conditions. Here an extension of the classic upslope model is presented, which incorporates an explicit representation in the vertical dimension, represents the finite growth time of hydrometeors, their downwind advection by the prevailing wind, and also allows for evaporation. For a simple mountain geometry the authors derive an analytical solution for the precipitation rate, which can be understood in terms of four nondimensional parameters. The finite growth time and slanting hydrometeor trajectories give rise to some interesting possibilities: a precipitation rate that maximizes at intermediate values of the horizontal wind speed, localized precipitation efficiencies in excess of 100%, and a reverse rain shadow with more precipitation falling on the leeward flank than on the windward flank.

## 1. Introduction

The influence of surface topography on patterns of precipitation leads to some of the most pronounced climate gradients on earth, reflected in sharp transitions in flora and fauna across many mountain ranges. Not only is orographic precipitation important for natural ecosystems and for the management of human water resources, but it also has significant interactions with other physical components of the earth system on a wide range of time scales. Over millions of years, for example, patterns of erosion, rock exhumation, and the form of mountain ranges themselves reflect patterns of precipitation (Beaumont et al. 1992; Willett 1999; Montgomery et al. 2001; Reiners et al. 2003; Anders et al. 2004, unpublished manuscript hereafter A04). During the Pleistocene the location of, and ice flux within, the great continental-scale ice sheets of the ice ages were controlled in part by patterns of snow accumulation (Sanberg and Oerlemans 1983; Kageyama et al. 1999; Roe and Lindzen 2001; Roe 2002). On shorter time scales, natural hazards such as avalanches and landslides are impacted by precipitation intensity in mountainous regions (e.g., Caine 1980; Conway and

Raymond 1993). So, while the existence of a rain shadow across a mountain range whose axis is perpendicular to the prevailing wind direction is one of the most confident expectations in atmospheric science, it is worthwhile to ask how, in different climates, patterns of orographic precipitation might change. In these contexts, it is to be hoped that simple representations of orographic precipitation can yield an understanding of the sensitivity of patterns to conceivable changes in forcing and that they can be implemented in investigations of these coupled systems.

Research efforts to categorize and model orographic precipitation have pursued an hierarchy of approaches, from statistical regressions (e.g., Nordø and Hjortnæs 1966; Daly et al. 1994; Wratt et al. 2000), to sophisticated mesoscale modeling, including complex microphysical schemes and in some instances resolving clouds (e.g., Katzfey 1995a,b; Colle et al. 1999; Rotunno and Ferretti 2001; Lang and Barros 2004; Smith et al. 2003). Intermediate approaches developing reduced models of orographic precipitation have also been pursued. These models have generally focused on the precipitation that ought to result from stable ascent, although it is important to note that observations also indicate that convection can modify patterns (e.g., Browning et al. 1974; Medina and Houze 2003). The simplest models (often referred to as upslope models) are essentially two-dimensional with streamlines everywhere parallel to the mountain (e.g., Sawyer 1956;

---

*Corresponding author address:* Dr. Gerard Roe, Dept. of Earth and Space Sciences, University of Washington, Seattle, WA 98195.

E-mail: gerard@ess.washington.edu

Smith 1979; Alpert 1986) and assume that the condensation rate is proportional to the rate of ascent of the air multiplied by the vertical gradient of the saturated moisture content. Therefore condensation, and thus precipitation, maximize over the steepest windward slopes. Another set of models aim to solve for the airflow in a more realistic way (e.g., Myers 1962; Smith 1979; Sarker 1966; Fraser et al. 1973; Colton 1976; Smith and Barstad 2004). It is commonly found in these models that some downwind smoothing of the condensation rate needs to be applied in order to get precipitation rates consistent with observations. It is argued that this smoothing reflects the growth and downwind advection of hydrometeors (precipitation particles large enough to fall). Demonstrating the potential of this mechanism, Hobbs et al. (1973) used computations of the airflow across a two-dimensional ridge and incorporated explicit calculations of hydrometeor trajectories. Their results showed that the concentration of the condensation ice nuclei and the growth process greatly affected the descent trajectories. A final category of diagnostic numerical models exist that, to varying degrees of complexity, diagnose the topographically modified atmospheric flow from the large-scale circulation and include formulations of precipitation formation (e.g., Colton 1976; Rhea 1978; Sinclair 1994; Barros and Lettenmeier 1993).

All of these models are proposed to some degree as generalized models of orographic precipitation. Data are hard to come by in mountainous terrains, so such models are often evaluated (or more typically calibrated) for a limited dataset, sometimes for a particular storm and sometimes for the climatological distribution. Indeed, Barros and Lettenmeier (1994a) argue for the necessity of a range-by-range calibration of any reduced precipitation model, asserting that the myriad factors controlling precipitation formation make the prevailing synoptic and microphysical conditions for each mountain range essentially unique.

The purpose of this paper is to develop a simple framework for the precipitation pattern in terms of a few model parameters, where the value of those parameters can be related to different precipitation situations. Our goal is to interpret precipitation patterns in terms of the prevailing wind, several cloud microphysics properties, and the dimensions of the mountain range. We concentrate on three main defining aspects, which together might be said to characterize the precipitation pattern: the maximum precipitation rate, the location of the maximum precipitation rate, and the strength of the rain shadow.

The model can be regarded as an extension of the classic upslope model, with an explicit representation in

the vertical that incorporates the conversion of condensate into hydrometeors, their terminal velocity and advection by the horizontal wind field, and leeside evaporation. It can also be modified to incorporate vertical wind shear. Within this reduced framework, an analytical solution is derived for the precipitation pattern, the dependency of which on four nondimensional parameters can be clearly ascertained. The chief costs of deriving this solution are a physically realizable atmospheric flow—simple mechanical lifting is assumed, which omits any gravity wave response or blocking of the flow—and a simplified mountain geometry. The results of this study can be contrasted with those of Smith and Barstad (2004; also Jiang and Smith 2003; Smith 2003) in which a solution is presented that accounts for linear atmospheric response to flow over topography, but in which moisture is represented in terms of a vertically integrated column and hydrometeor growth and fallout occurs on a characteristic time scale. Many of the aspects of the patterns are similar but in some cases the physical reasons are different. These are highlighted. The discussion identifies the aspects left out of our model formulation that likely result in the largest departure from nature.

The model simplifications probably preclude it from being applied to simulate a set of observations, nor is that intended. It is a framework within which the effects of slanting hydrometeor trajectories and mountain geometry on the pattern of precipitation can be explored. In this regard, the model continues from the work of Hobbs et al. (1973), who demonstrated the importance of these effects. It is also in contrast to many other simple models of orographic precipitation, which integrate the condensation rate in a vertical column above the mountain slopes. The condensation rate in these models is thus distributed on the landscape in a fundamentally different way from that in the model presented here.

## 2. The model

### a. Mountain geometry

The model framework is illustrated in Fig. 1. Atmospheric flow impinges on a wedge-shaped mountain described by the function  $z_s(x_s)$ ,

$$\begin{aligned} z_s &= \frac{H}{L_1}(L_1 + x_s), & -L_1 < x_s \leq 0 \\ z_s &= \frac{H}{L_2}(L_2 - x_s), & 0 < x_s \leq L_2 \\ z_s &= 0, & \text{elsewhere.} \end{aligned} \quad (1)$$

If  $L_1 \neq L_2$ , the wedge is asymmetric.

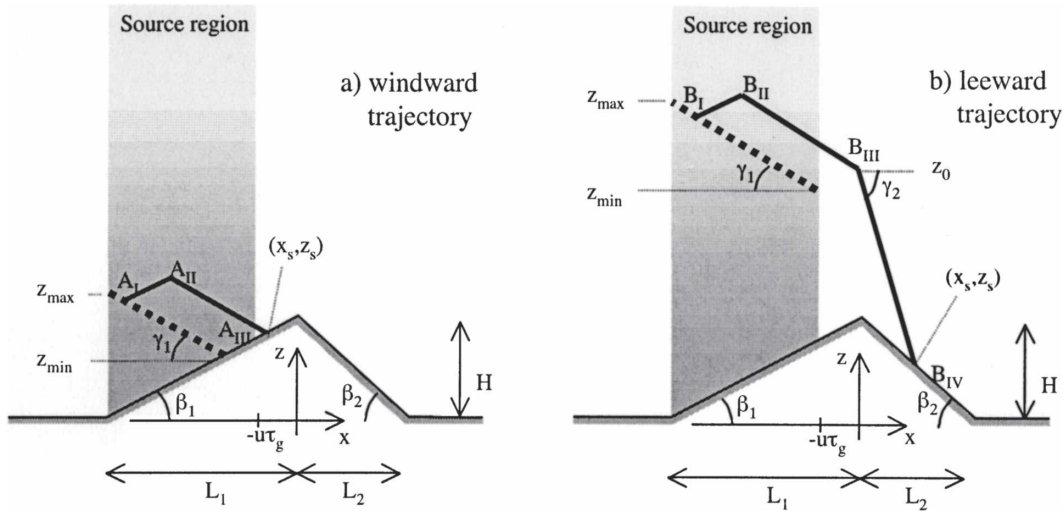


FIG. 1. Schematic illustration of model framework. Black lines are hydrometeor trajectories. The dashed lines are source lines that delineate all points within the source region where condensation ends up as precipitation at the same surface point. See text for more details.

*b. Airflow*

Our model is time independent. The incoming air is assumed to be moving at constant speed, neutrally stratified, and saturated. We further assume that flow undergoes mechanically forced ascent on the windward flank and forced descent to the lee. Thus the rate of vertical ascent (or descent) is given by the strength of the prevailing wind multiplied by the slope (i.e.,  $w = u dz_s/dx_s$ ), independent of height. Strictly, such a flow response could only be possible for a neutrally stable atmosphere in which the horizontal scales are much larger than the vertical scales. In reality, changes in vertical motion (e.g., crossing from the windward to the leeward flank) cause vertical accelerations that, in a stably stratified fluid, set up gravity waves that propagate away from the source (e.g., Smith 1979, 2003; Durran 1986, 2003, Colle 2004). Gravity waves will cause the biggest departure from the mechanically forced response for small steep mountain ranges, weak flow regimes, or strongly stable conditions when the modification of the flow by the gravity wave response would be largest. In the context of orographic precipitation, a sense of the departure from the mechanically forced pattern is presented in the work of Hobbs et al. (1973), Smith and Barstad (2004), and Colle (2004). Omitting gravity waves precludes, for example, any lifting upwind of the mountain. They can also trigger unstable convection, which can modify precipitation patterns (e.g., Browning et al. 1974; Medina and Houze 2003). Moist neutral, or near-neutral, flows have been shown to be relevant to orographic precipitation in several

recent studies (e.g., Rotunno and Ferretti 2001; Medina and Houze 2003).

We will discuss the consequences of a more realistic flow response in section 5. A third effect of stable stratification is that for smaller horizontal scales the influence of the mountain on the circulation decays with height (e.g., Durran 1986). This last aspect can be incorporated into the model by the choice of moisture scale height described below.

*c. Condensation rate*

On the windward flank, the ascent of saturated air leads to a steady condensation rate per unit volume,  $S$ , which can be written as

$$S[\text{kg m}^{-3} \text{s}^{-1}] = \frac{d(\rho q_s)}{dz} \frac{dz}{dt} \tag{2}$$

Here,  $q_s$  is the saturation specific humidity,  $dz/dt$  is the vertical velocity, and  $\rho$  is the density of air. This expression can be developed using the relations

$$dz/dt = w_1 = u \frac{dz_s}{dx_s} = uH/L_1,$$

and also by making an exponential approximation for the specific humidity so that  $\rho(z) q_s(z) = \rho_0 q_0 \exp(-z/H_m)$ , independent of  $x$ ;  $\rho_0$  and  $q_0$  are the density and the saturation specific humidity at  $z = 0$ , and  $q_0$  is a function of surface temperature and pressure. Here  $H_m$  is the moisture scale height and typically varies between  $\sim 2$  and  $\sim 4$  km, being greatest in the Tropics (e.g., Peixoto and Oort 1992), and could also be regarded as

incorporating the decrease with height of the influence of the mountain on the atmospheric flow. Hence (2) can be rewritten as

$$S(z) = \frac{\rho_0 q_0 u H}{H_m L_1} e^{-z/H_m}. \quad (3)$$

Condensation occurring at altitude reaches the ground only after cloud droplets are converted to hydrometeors and only after those hydrometeors have reached the ground. (In this discussion we use terms appropriate to warm clouds. Our model, however, is applicable to mixed phase and/or entirely glaciated clouds, which we represent by different choices of model parameters. We do not consider clouds with a phase change with altitude although our framework allows for this extension.) We assume that a finite period of time,  $\tau_g$ , must elapse for the growth of cloud droplets to form hydrometeors and that, thereafter, they fall with a characteristic terminal velocity,  $v_f$ . In essence this assumes a single representative size scale for hydrometeors and, so, neglects any size distribution. Collection or coalescence of cloud water droplets on the way down is also not treated explicitly, so the changes in the trajectories that this mass accumulation results in are not included either. These assumptions give the following characteristic pathways, or trajectories, for the falling hydrometeors depending on whether the precipitation ends up falling on the windward or leeward flanks of the range, illustrated in Figs. 1a,b. For the windward flank

- $A_I$  to  $A_{II}$ : growth of droplets during which they are carried with the ascending flow.
- $A_{II}$  to  $A_{III}$ : hydrometeors fall through ascending air, no evaporation.

For the leeward flank

- $B_I$  to  $B_{II}$ : as for  $A_I$  to  $A_{II}$ .
- $B_{II}$  to  $B_{III}$ : as for  $A_{II}$  to  $A_{III}$ .
- $B_{II}$  to  $B_{IV}$ : hydrometeors fall through descending air, some evaporation occurs.

Finally, for  $x_s > L_2$ , the last part of the trajectory is through air with no vertical velocity.

These assumptions result in a source region on the windward flank. Because of the finite formation time for hydrometeors, it ends at  $x = -u\tau_g$  (as indicated by Fig. 1). The finite growth time also means that no precipitation reaches the ground for  $x_s < -L_1 + u\tau_g$ . For every point on the surface downwind of this, a source line can be defined as the locus of points in the source region from which condensation ends up as precipitation at that surface point. Examples are shown as dashed lines in Figs. 1a,b.

The total condensation rate integrated along any source line can be written as

$$\int_{\text{source}} S(z) dl = \int_{z_{\min}}^{z_{\max}} S(z) \left[ 1 + \left( \frac{dx}{dz} \right)^2 \right]^{1/2} dz. \quad (4)$$

Here  $dl$  is an infinitesimal increment along the source line, and  $z_{\min}$  and  $z_{\max}$  are the intersections of the source line with the boundaries of the source region. To convert this integral into the precipitation rate,  $R(x_s)$ , we note that (4) gives the precipitation flux per unit area perpendicular to the direction of the source line, and a geometric factor needs to be included to convert this into a flux per unit area in the horizontal. Moreover, for points to the lee of the range crest, evaporation of falling hydrometeors can be crudely and simply incorporated according to the time spent outside of the orographic cloud: precipitation exponentially diminishes with a characteristic time scale,  $\tau_{ev}$ . Incorporating these two aspects, the precipitation rate per unit horizontal area can be written as

$$R(x_s) = \left( \frac{\tan\beta_1}{\tan\gamma_1} + 1 \right) \int_{z_{\min}}^{z_{\max}} S(z) dz \quad \text{for} \\ -L_1 + u\tau_g < x_s \leq 0 \quad (5a)$$

$$R(x_s) = \left( \frac{\tan\gamma_2 - \tan\beta_2}{\tan\gamma_1} \right) \exp\left( -\frac{z_0 - z_s}{\tau_{ev}v_f} \right) \\ \times \int_{z_{\min}}^{z_{\max}} S(z) dz \quad \text{for } 0 < x_s \leq L_2 \quad (5b)$$

$$R(x_s) = \left( \frac{\tan\gamma_3}{\tan\gamma_1} \right) e^{-\frac{z_0 - z_s}{\tau_{ev}v_f}} \int_{z_{\min}}^{z_{\max}} S(z) dz \quad \text{for } L_2 < x_s, \quad (5c)$$

where  $z_0$  is the altitude of the point where the trajectory crosses the crest (i.e., at  $x = 0$ ). The  $\beta$  are the windward and leeward mountain slopes, and the  $\gamma$  are the angles of the hydrometeor trajectories make to the horizontal (Fig. 1). Note the evaporation factor can be omitted entirely by setting  $\tau_{ev} = \infty$ . In the absence of evaporation water is conserved: all condensation occurring within the source region ends up as precipitation at the surface.

Equation (5) uses the source lines in Fig. 1, which are dictated by hydrometeor growth times and trajectories, to map condensation occurring in the source region onto precipitation falling at the surface. Thus the determination of the precipitation rate at a surface point requires calculation of the source line for that point in order to find the appropriate  $z_{\max}$  and  $z_{\min}$ . The equations for the source lines and expressions for  $z_{\max}$  and  $z_{\min}$  are developed in appendix A.

For the windward flank there is no evaporation ( $\tau_{ev} = \infty$ ), and combining Eqs. (3), (5a), (A8), (A10) gives

$$R(x_s) = \frac{\rho_0 q_0 u H}{L_1} \left( \frac{\frac{L_1 v_f}{uH}}{\frac{L_1 v_f}{uH} - 1} \right) \times \left[ \exp\left(-\frac{z_{\min}}{H_m}\right) - \exp\left(-\frac{L_1 v_f z_{\min}}{uH H_m}\right) \right] \tag{6a}$$

$$z_{\min} = z_s - \frac{u \tau_g H}{L_1}. \tag{6b}$$

For the leeward flank, (3), (5b) or (5c), (A11), and (A13) give

$$R(x_s) = \frac{\rho q_0 u H}{L_1} \left( \frac{\frac{L_1 v_f}{uH}}{\frac{L_1 v_f}{uH} - 1} \right) \exp\left(-\frac{x_s}{u \tau_{ev}}\right) \times \exp\left(-\frac{z_{\min}}{H_m}\right) \times \left\{ 1 - \exp\left[-\frac{v_f}{H_m u} (L_1 - u \tau_g) \left(1 - \frac{uH}{v_f L_1}\right)\right] \right\} \tag{7a}$$

$$z_{\min} = H + \frac{x_s v_f}{u} - \frac{u \tau_g H}{L_1}. \tag{7b}$$

*d. Nondimensionalization*

Equations (6) and (7) nondimensionalize naturally by introducing five physically meaningful parameters. Subscripts (1, 2) denote windward and leeward sides, respectively:

- $R_0 \equiv \frac{\rho_0 q_0 u H}{L_1}$  Vertically integrated condensation rate in a windward air column.
  - $\theta_{1,2} \equiv \frac{L_{1,2} v_f}{uH}$  The ratio of the raindrop trajectories slope to the orographic slopes.
  - $\alpha \equiv \frac{H}{H_m}$  The ratio of mountain height to moisture scale height.
  - $\psi_{1,2} \equiv \frac{L_{1,2}}{u \tau_g}$  The ratio of mountain length to the formation length scale.
  - $\xi \equiv \frac{H}{v_f \tau_{ev}}$  The ratio of mountain height to the evaporation height scale.
- (8)

A sixth parameter,  $L_1/L_2$ , could be introduced that would govern the asymmetry of the mountain range.

The system would then be described completely in non-dimensional terms, but for the sake of clarity we leave this last parameter out of the equations shown.

The precipitation equations can be expressed in terms of these parameters [after a lot of rearrangement and substituting from (1) for the shape of the mountain].

For  $-1 + \frac{1}{\psi_1} < \frac{x_s}{L_1} \leq 0$ :

$$R(x_s) = R_0 \left( \frac{\theta_1}{\theta_1 - 1} \right) \left\{ \exp\left[-\alpha \frac{z_{\min}}{H}\right] - \exp\left[-\theta_1 \alpha \frac{z_{\min}}{H}\right] \right\} \tag{9a}$$

$$\frac{z_{\min}}{H} = 1 - \frac{1}{\psi_1} + \frac{x_s}{L_1}. \tag{9b}$$

For  $\frac{x_s}{L_2} > 0$ :

$$R(x_s) = R_0 \left( \frac{\theta_1}{\theta_1 - 1} \right) \exp\left(-\theta_2 \frac{\xi x_s}{L_2}\right) \exp\left(-\alpha \frac{z_{\min}}{H}\right) \times \left\{ 1 - \exp\left[-\alpha \left(1 - \frac{1}{\psi_1}\right) (\theta_1 - 1)\right] \right\} \tag{10a}$$

$$\frac{z_{\min}}{H} = 1 - \frac{1}{\psi_1} + \theta_2 \frac{x_s}{L_2}. \tag{10b}$$

These parameters have the following physical constraints. For precipitation to fall at all, the terminal velocity must exceed the vertical velocity of the air, which requires that  $\theta_1 > 1$ . As the source lines get closer to horizontal  $\theta_1$  tends to 1, but  $z_{\max}$  tends to  $z_{\min}$ , so  $R(x_s)$  remains finite (as it must physically). A second constraint, necessary for any precipitation to occur, is that the windward width must be greater than the growth length scale:  $\psi_1 > 1$ . This is related to the autoconversion limit argued for by Robichaud and Austin (1988) in which cloud water within the orographic cloud produces precipitation without an external seeder cloud. It is also the threshold behavior, noted in Jiang and Smith (2003), in which cloud droplet conversion must occur during the residence time within the source region. The seeder-feeder mechanism can be imitated in this model by taking a short growth time, which leads to efficient rain out on the windward flank (e.g., Sinclair 1994).

**3. Results**

To present the basic precipitation pattern we take the following set of parameters:  $H = 2.5$  km,  $L_{1,2} = 30$  km,

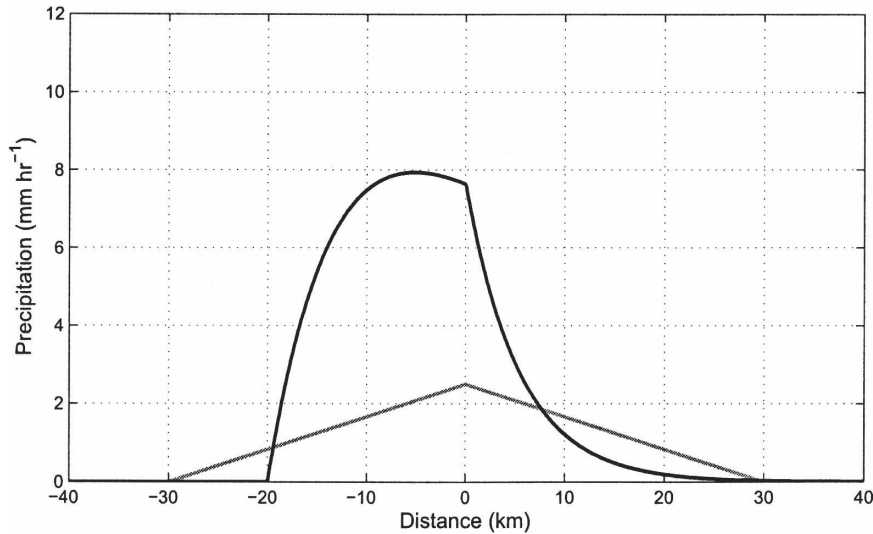


FIG. 2. Precipitation pattern for standard choice of parameters (equal to midvalues in Table 1). Topography is shown as gray line.

$u = 10 \text{ m s}^{-1}$ ,  $v_f = 4.0 \text{ m s}^{-1}$ ,  $\tau_g = 1000 \text{ s}$ ,  $\tau_{ev} = 2000 \text{ s}$ ,  $H_m = 3.0 \text{ km}$ , and  $q_0 = 4.0 \text{ g kg}^{-1}$ . Appendix B provides justification for these choices from microphysical calculations. They are also broadly consistent with observations in case studies of orographic precipitation (e.g., Sinclair 1994; Smith and Barstad 2004). Colle (2004) integrates a mesoscale forecast model in a two-dimensional (height-width) setup.

The pattern is shown in Fig. 2. Because of the finite growth time, precipitation is offset from the toe of the windward flank. It increases rapidly to a rate of about  $8 \text{ mm h}^{-1}$ , about halfway along the windward flank. There is a gradual drop-off toward the crest, which is followed by a much stronger decrease after crossing to the lee, becoming negligible for  $x_s > \sim 20 \text{ km}$ . This shape is consistent with the quintessential pattern for orographic precipitation on large mountain ranges, found in numerous observational and modeling studies. The sharp kink in the pattern at the divide reflects the triangular shape of the topography. For a topographic slope equivalent to ours, Colle (2004) find maximum precipitation rates between  $3$  and  $13 \text{ mm h}^{-1}$  for winds varying between  $10$  and  $30 \text{ m s}^{-1}$  for their weak atmospheric stability cases. Comparing Fig. 2 with Colle (2004), significant spill-over precipitation reaches over about the same distance beyond the divide. The biggest difference with Colle (2004) is the absence of significant precipitation upwind of the topography. In Colle (2004) (and also Smith and Barstad 2004) this occurs because of ascent of air windward of the mountain due to the dynamical response of the atmosphere.

A frequently employed description of orographic

precipitation is precipitation efficiency, PE (e.g., Smith 1979; Smith et al. 2003). It can be defined at each point as the actual precipitation rate divided by the vertically integrated condensation rate above that point if the vertical velocity everywhere equaled its value at the surface. This measure emerges naturally from our analyses as

$$\text{PE} = \frac{R(x_s)}{R_0} e^{z_s/H_m}. \quad (11)$$

Because of the finite growth time, advection, and slanting hydrometeor trajectories in the model, it is possible for localized precipitation efficiency to exceed 100% (see also Smith and Barstad 2004). For the standard case, precipitation efficiency actually reaches 145%. (That is, the precipitation at the ground at a given location can be greater than the total amount of water condensed in the vertical column above. This highlights the nonphysical nature of the localized precipitation efficiency.) Averaged over the windward domain, however, it is 65%, which is not atypical in observations (e.g., Sawyer 1956; Myers 1962; Colton 1976; Smith et al. 2003). Sensitivity studies in section 3a show that a wide range of precipitation efficiencies is possible (Fig. 3). But, all else being equal, smaller mountains (height and/or width) have lower precipitation efficiencies, which is consistent with the observations cited above and, for example, Robichaud and Austin (1988) and Jiang and Smith (2003).

The location of the maximum precipitation rate can be understood directly from Fig. 1; it will be at the

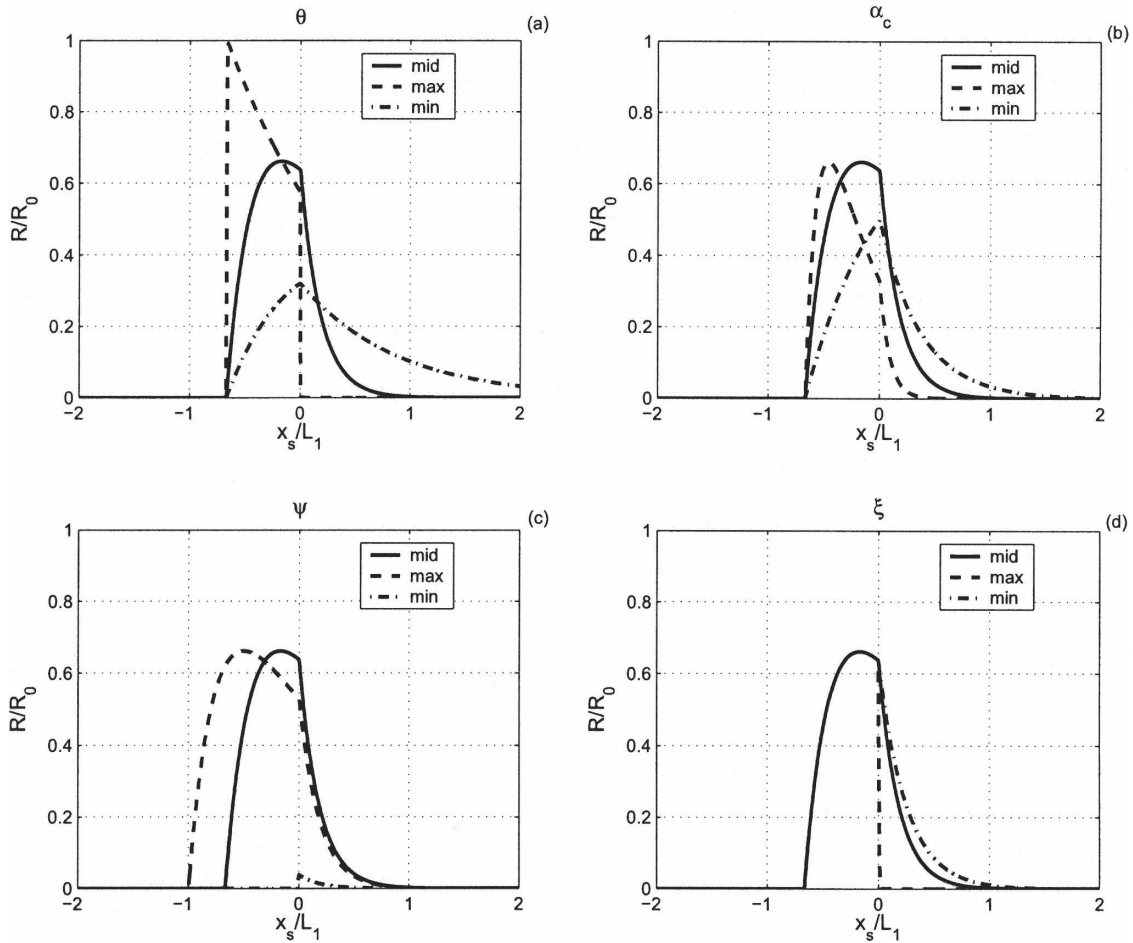


FIG. 3. Sensitivity of precipitation pattern (i.e.,  $R/R_0$ ) to variations in nondimensional parameters. Different panels show sensitivity to the different parameters. Each panel shows the effect of varying the indicated parameter across its range of plausible values (given in Table 2), while all other parameters are held at their midrange values. See the text for more details. Note that precipitation efficiency can be inferred from this figure: it is equal to  $R/R_0 \exp(z_s/H)$ , and for (a)  $\theta_{\max}$  it is close to 100%. (b), (c) When the precipitation maximum is offset from the crest, its magnitude does not depend on  $\alpha$  or  $\psi$ .

surface point with the longest, moistest source line, which for the assumptions and geometry of the model means it will always occur on the windward flank. We compute

$$\frac{d}{dx_s} (R(x_s)/R_0)$$

from (9) and set it to zero to find

$$\left. \frac{x_s}{L_1} \right|_{\max} = \min \left\{ 0, -1 + \frac{1}{\psi_1} + \frac{\ln \theta_1}{\alpha(\theta_1 - 1)} \right\}. \quad (12)$$

If the growth time is sufficiently large that the growth phase occurs over a large fraction of the windward flank (i.e.,  $\psi_1$  tends to 1), the width of the source region decreases and the maximum precipitation rate tends to occur close to the divide. For small values of the pa-

rameters (i.e.,  $\alpha, \theta - 1 \lesssim 3$ ), the location of the maximum is most sensitive to  $\alpha$ . That is, when the slopes of hydrometeor trajectories are almost as steep as the mountain slopes, the most effective way to shift the location of the precipitation maximum is by changing the ratio of the moisture height scale to the mountain height. Conversely, for large values of  $\theta$  and  $\alpha$ , the sensitivity to  $\theta$  dominates.

The value of the maximum precipitation rate can be found by substituting (12) into (9):

$$R_{\max} = \frac{R_0 \theta_1}{(\theta_1 - 1)} \left\{ \exp \left( -\frac{\ln \theta_1}{\theta_1 - 1} \right) - \exp \left( -\frac{\theta_1 \ln \theta_1}{\theta_1 - 1} \right) \right\}$$

for  $\left. \frac{x_s}{L_1} \right|_{\max} < 0,$

$$R_{\max} = \frac{R_0 \theta_1}{(\theta_1 - 1)} \left\{ \exp \left[ -\alpha \left( 1 - \frac{1}{\psi_1} \right) \right] - \exp \left[ -\theta_1 \alpha \left( 1 - \frac{1}{\psi_1} \right) \right] \right\} \text{ for } \left. \frac{x_s}{L_1} \right|_{\max} = 0. \quad (13)$$

Interestingly, if it is not located at the crest, the maximum precipitation rate does not depend on either  $\alpha$  or  $\psi_1$  even though its location does (shown in Fig. 3). This is because the value of  $\psi_1$  does not affect the location of the source line giving maximum precipitation, and the maximum difference between two exponentials of the form of (9a) depends only on the factor by which the exponents differ (and thus not on  $\alpha$ ). In contrast, when the precipitation maximum is located at the crest, its magnitude decreases when either the growth time increases or the moisture scale height decreases.

#### a. Sensitivity of precipitation pattern to parameter variations

Table 1 gives a range of plausible physical parameters with low, mid, and high values. By selecting from these values, we can create low, mid, and high values for each of the nondimensional parameters, shown in Table 2, and adjust where extreme values would be outside the bounds of physically meaningful solutions. The results are shown in Fig. 3 and discussed below.

The precipitation pattern is most sensitive to plausible variations in  $\theta_{1,2}$  (the ratio of mountain slopes to trajectory slopes). If the surface slopes are shallow compared to the hydrometeor trajectories ( $\theta_{1,2}$  large), most of the precipitation occurs on the windward flank. In this case, precipitation efficiency is close to 100%. Conversely for low values of  $\theta$  (e.g., from strong horizontal winds or low fall speeds), trajectories are shallow and precipitation is carried far over the divide. This is essentially the behavior noted and explained by Hobbs et al. (1973) for the Cascades in Washington State. Note

TABLE 1. Table of dimensional parameters used in model sensitivity analysis. Appendix B presents microphysical calculations for warm rain, graupel, and lightly rimed ice used to guide these ranges. For simplicity a symmetric mountain was assumed.

Parameter (units)	Symbol	Low	Mid	High
Mountain height (km)	$H$	1.0	2.5	4.0
Mountain width (km)	$L_1, L_2$	10	30	100
Wind speed ( $\text{s}^{-1}$ )	$u$	1.0	10.0	30.0
Terminal fall speed ( $\text{m s}^{-1}$ )	$v_f$	1.0	4.0	8.0
Growth time (s)	$\tau_g$	200	1000	2000
Evaporation time scale (s)	$\tau_{ev}$	100	2000	Inf
Moisture height scale (km)	$H_m$	2.0	3.0	4.0

TABLE 2. Table of nondimensional parameters calculated from values in Table 1 and Eq. (8). An asterisk denotes a value that was adjusted to the minimum value needed to get a physically meaningful precipitation pattern.

Parameter	Low	Mid	High
$\theta_1, \theta_2$	1.01*	4.8	800
$\psi_1, \psi_2$	1.01*	3.0	500
$\xi$	0	0.31	40
$\alpha$	0.25	0.83	2.0

also that the precipitation efficiency plummets in this case. The value of  $\alpha$  also affects the pattern considerably. Where the moisture height scale is deep compared to the mountain height scale, precipitation maximizes at or near the crest, and the rain shadow is not strong. If moisture is confined to low elevations, the source line for the crest accesses low moisture air, and the precipitation rate maximizes far down on the windward flank.

The hydrometeor growth time has an impact on the pattern when  $u\tau_g$  is comparable to the mountain half-width. In this case, precipitation is significantly displaced from the foot of the windward flank, and the maximum occurs at the crest. Moreover, because of the restricted width of the source region, points to the lee of the mountain sample air at relatively high altitude, and consequently there is a rapid drop-off of precipitation to the lee. Evaporation impacts only the leeward pattern by construction, but it can have an important impact on the strength of the rain shadow if its characteristic time scale is comparable to the fall time of the hydrometeors.

We next present results from a somewhat broader range of parameter choices, focusing on three aspects of the precipitation pattern: the maximum precipitation rate, the location of the maximum, and the strength of the rain shadow. We refer to section 5 and to Colle (2004) and Smith and Barstad (2004) for a description of how parameter variations can lead to dynamically induced changes in the precipitation pattern.

#### b. Maximum precipitation rate

Figure 4 shows contours of the maximum precipitation as a function of  $u$  and  $v_f$ , and of  $H$  and  $L_{1,2}$ . Interestingly, for a given fall speed  $v_f$ , the maximum precipitation rate reaches its largest value at an intermediate value of  $u$ . This is fundamentally due to the model framework representing the vertical dimension. As  $u$  increases from small values, the condensation rate increases because of greater ascent on the windward flank. However advection increases too. This reduces the width of the source region and the slopes of the source lines and hydrometeor trajectories become shall-

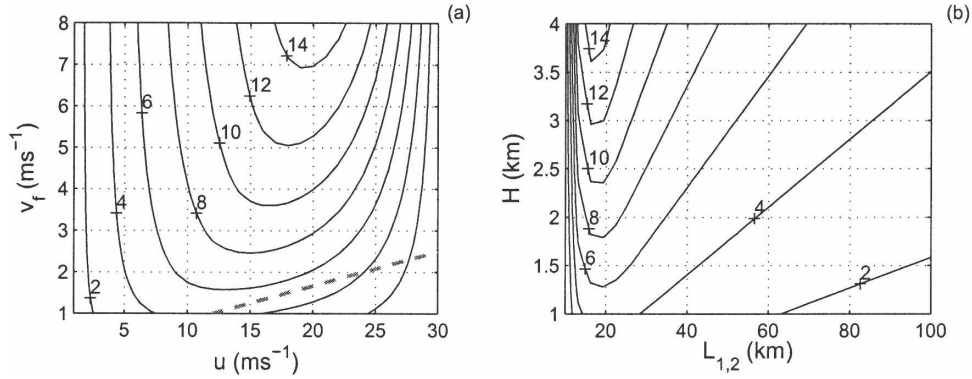


FIG. 4. Sensitivity of the maximum precipitation rate to plausible variations in parameters. Shown are contours of the maximum precipitation rate as a function of (a)  $u$  and  $v_f$ , (b)  $L_{1,2}$  and  $H$ . In each panel all other values were held at their standard values. In (a) the area underneath the dashed gray line has  $\theta < 1$ , and so values are not meaningful. Contour interval is  $2 \text{ mm h}^{-1}$ .

lower (Fig. 1). This has two effects: the lengths of source lines decrease, which reduces the line integral [i.e., Eq. (5)], and more hydrometeors formed at altitude are advected over the crest. As wind speeds increase, these effects come to dominate over the increased condensation rate. This is particularly pronounced at low values of  $v_f$  (Fig. 4a), suggesting the effect may be stronger for snowfall than for rain. Demonstrating this behavior, the precipitation patterns for three values of  $u$  are shown in Fig. 5. A similar although subtler effect can be seen in Fig. 4b: for a given mountain height there is an optimum half-width ( $L_1$ ) for the precipitation rate, caused again by the decreasing length of the source region for a finite growth time. Figure 4b also shows that away from this small  $L_1$  re-

gime, the maximum precipitation is the same for mountains of the same surface slope. But importantly we note that, in contrast to a simple upslope model (i.e., precipitation proportional to slope), changes in surface slope do not produce proportional changes in maximum precipitation rate.

*c. Location of maximum precipitation*

The location of the maximum precipitation rate is, not surprisingly, sensitive to the value of  $u$ , but only up to the value at which the precipitation maximum reaches the crest (Fig. 6a). Depending on the value of  $v_f$  (and of course the dimensions of the mountain), the precipitation maximum may be at the crest for a wide range of  $u$ . This result has some potential value: in such

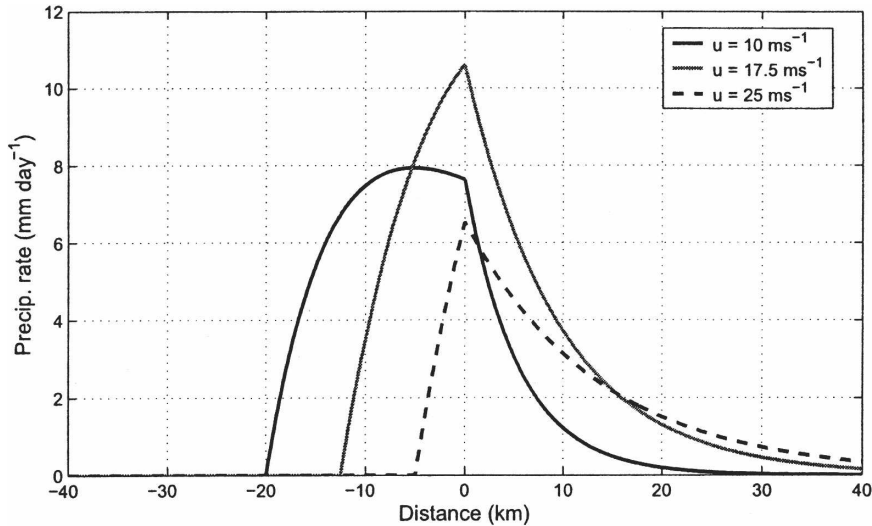


FIG. 5. Precipitation pattern as a function of  $u$ . All other parameters at standard values. The maximum precipitation rate attains its largest value at an intermediate value of  $u$ .

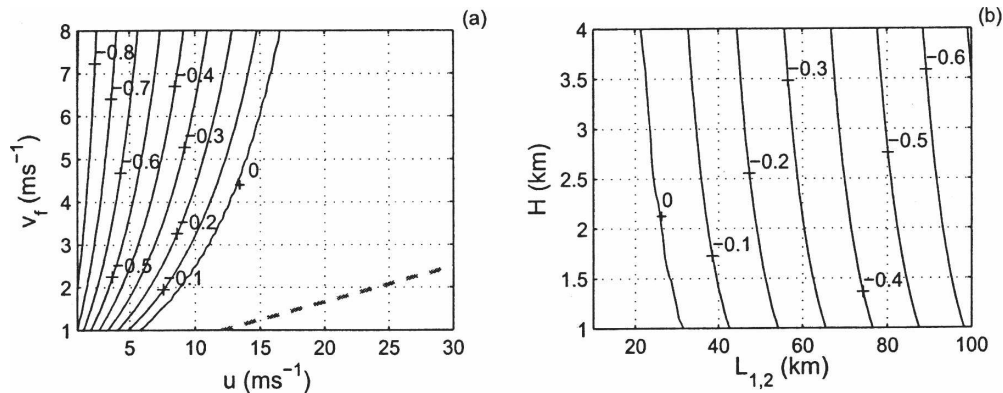


FIG. 6. Sensitivity of the location of the maximum precipitation rate to plausible variations in parameters. As in Fig. 4 but contours are of the location of the maximum precipitation rate [i.e.,  $(x_s/L_1)_{\max}$ ]. A value of  $-1$  means the maximum precipitation rate is at the toe of the windward flank, a value of  $0$  means it is at the crest.

a regime, the pattern of the precipitation would be robust under a wide variety of storm strengths. The location of the maximum does not depend strongly on the mountain height but is sensitive to the half-width (Fig. 6b).

#### d. Strength of rain shadow

The strength of the rain shadow is determined by integrating (9) and (10) to give the total precipitation falling on the windward and leeward flanks,  $P_W$  and  $P_L$ , respectively. The resulting expressions are given in section c of appendix A, and Figs. 7a,b shows their ratio,  $P_W/P_L$ , as a function of  $u$  and  $v_f$ ,  $\tau_g$  and  $\tau_{ev}$ . On its own,  $P_W$  looks a lot like the maximum precipitation rate: as  $u$  increases,  $P_W$  increases up to a maximum and then decreases as precipitation is increasingly advected over the divide. Consequently,  $P_L$  continues to increase un-

til, for very strong winds, significant precipitation gets advected beyond even the leeward flank. The strength of the rain shadow thus decreases as  $u$  increases. Interestingly, for high wind speeds or low fall speeds, there is a substantial region of parameter space where the rain shadow is reversed ( $P_W/P_L < 1$ ). As is to be expected, the rain shadow is stronger for higher fall speeds.

For our standard mountain, the strength of the rain shadow is relatively insensitive to variations of the growth and evaporation time scales (Fig. 7b) over the range considered. Of course,  $P_W$  is independent of  $\tau_{ev}$ , and only weakly dependent on  $\tau_g$ . For smaller mountain ranges than our standard case,  $P_W$ , and, hence the rain shadow, is much more sensitive to  $\tau_g$  (not shown). Evaporation does have the potential to significantly affect the rain shadow when the evaporation height scale

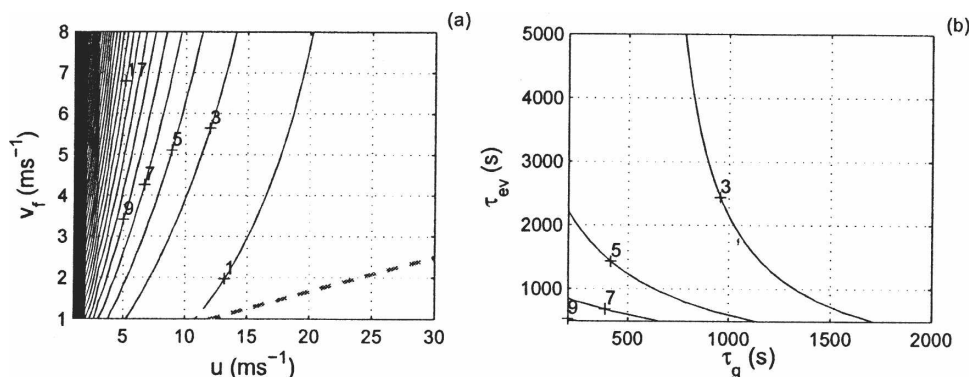


FIG. 7. Sensitivity of rain shadow to plausible variations in selected parameters. Graphs show contours of the total precipitation on the windward flank divided by the total precipitation on the leeward flank,  $P_W/P_L$ , for (a) varying  $u$  and  $v_f$  and (b) varying  $\tau_g$  and  $\tau_{ev}$ . Otherwise all values held at standard values. Note in (a) that the rain shadow is reversed (i.e., more precipitation on leeward flank) for  $P_W/P_L < 1$ .

$(v_f \tau_{ev})$  is comparable to the mountain height scale, which means  $\tau_{ev} \sim 600$  s in Fig. 7b.

**4. Other aspects of the precipitation pattern**

*a. Vertical wind shear*

So far we have not considered the effects of vertical wind shear, which causes condensate formed at higher elevations to be advected even further than that formed at low levels (e.g., Colle 2004). This stretches out the precipitation pattern, shown schematically in Fig. 8. In appendix C the equations for source lines are derived in the case of uniform vertical shear and  $\tau_g = 0$ . The geometrical factors multiplying the integrals in (5) are no longer constant with height. They are replaced by their mean values, which is a reasonable approximation provided  $\theta \geq 3$ . Figure 9 shows the calculated precipitation pattern for the standard parameter set and a vertical shear of  $0.003 \text{ s}^{-1}$ . The peak precipitation rate is reduced by around 25%, and the downwind precipitation rate increases appreciably. We note that just calculating trajectories does not take into account how vertical shear would change the condensation rate in the source region (or, in a fuller treatment, the impacts of changes on the phase and amplitude of gravity waves).

Since typical uses of a simplified model like this might mean that wind speed at only one level is specified, it is useful to ask if the effect of vertical shear can be imitated by changing the value of one of the other parameters. Changing the value of  $u$  does not work because it has an effect on both the distribution and amplitude of the precipitation rate (Fig. 9b). By analogy with  $\theta$  the natural nondimensional parameter is

$$\phi = \frac{Lv_f}{(u_0 + u_z H_m)H}. \tag{14}$$

For the shear case with  $u_z = 3 \times 10^{-3} \text{ s}^{-1}$  and standard parameters,  $\phi = 0.25$ . Without shear  $v_f$  must be equal to  $2.1 \text{ m s}^{-1}$  to produce the same  $\phi$ . Figure 9c shows that this value of  $v_f$  quite closely reproduce the effects of wind shear, although the location of the precipitation maximum is offset.

In the model development we have neglected coalescence of falling hydrometeors, a major effect of which is to increase fall speeds during descent. The resulting parabolic trajectories would be similar to those shown in Figs. 8 and B1. The results in Fig. 9 suggests such effects may be emulated by tuning the value of  $v_f$ .

*b. Asymmetry of mountain range*

Last, we present the precipitation patterns for asymmetric mountain ranges. Figure 10 shows the pattern

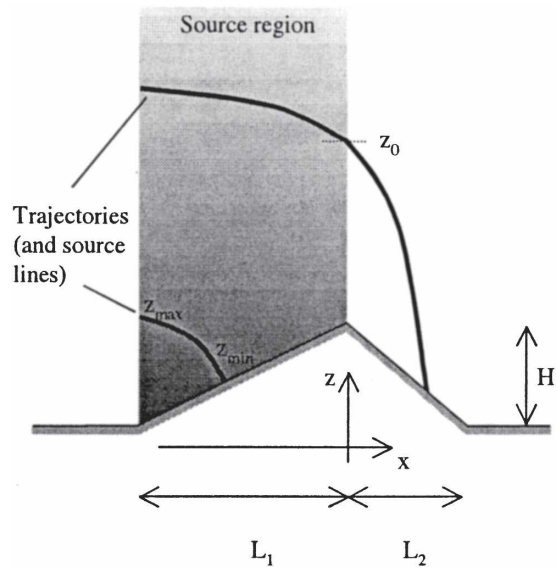


FIG. 8. Schematic illustration of hydrometeor trajectories including vertical wind shear. Zero growth time is assumed, so source lines and trajectories are coincident.

resulting from the standard parameter set but with  $L_1/L_2 = 1/3, 1,$  and  $3$ . If the height and total width of the mountain range are fixed, the asymmetry of the mountain shape controls the steepness of the windward slopes, the condensation rate via (3), and in turn the location and magnitude of the maximum precipitation rate. As the asymmetry varies, changes in windward slope are offset by changes in the source region width. In the case of no growth time and no evaporation these exactly balance, and total precipitation reaching the surface remains constant. This must be so since the total lifting of the column is a function of crest height only. However a finite growth time means that the narrower the windward flank (such as the Southern Alps in New Zealand), the narrower the source region width, and so less the total precipitation that falls as is seen in Fig. 10. Note though, that the maximum precipitation rate is largest for the narrow windward flank.

**5. Summary and discussion**

We have sought to characterize the microphysical and geometrical controls on patterns of orographic precipitation. The model presented is an extension of the classic upslope model to include a representation of the vertical dimension, and to account for both the growth time for hydrometeors and their advection by the prevailing wind. In essence the model is best thought of as providing scaling relationships for the pattern and allowing for a straightforward evaluation of the relative

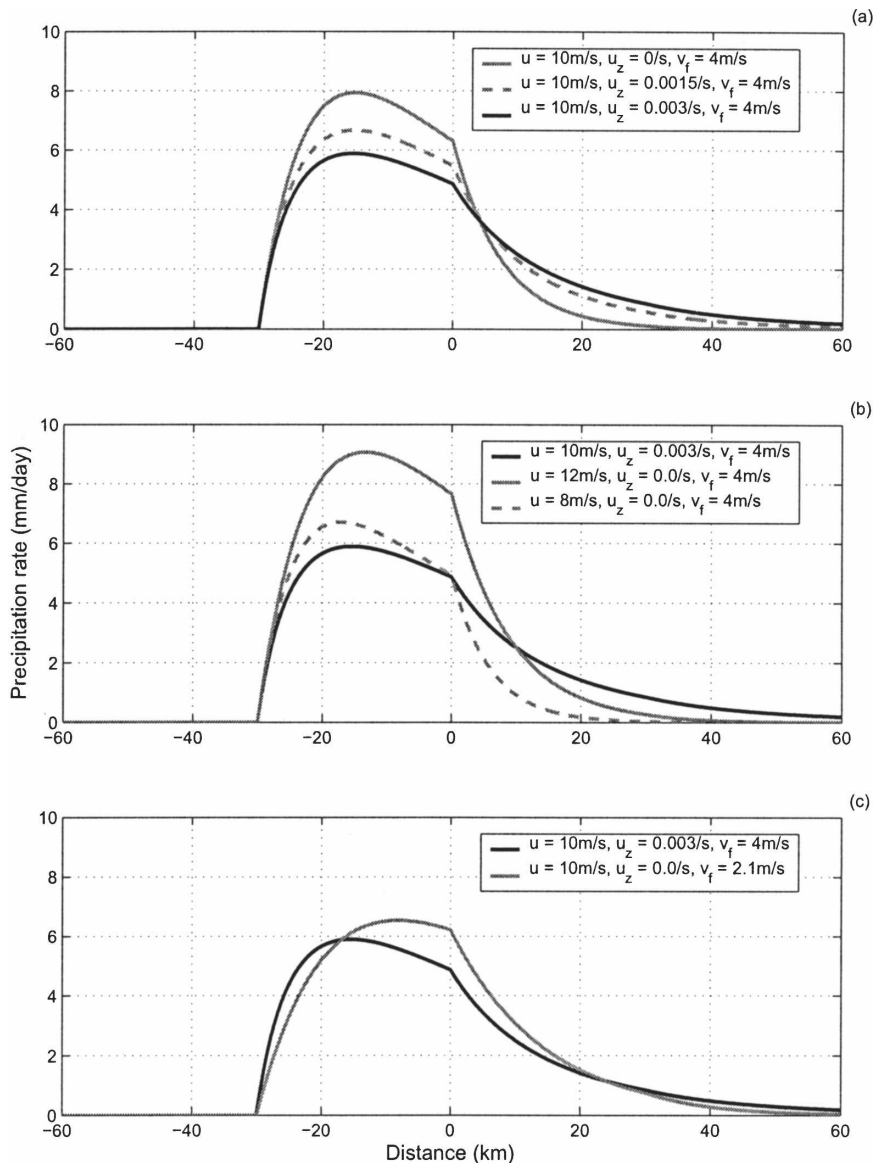


FIG. 9. Effect on the precipitation pattern of adding vertical wind shear. Standard parameters are used except for  $\tau_g = \tau_{ev} = 0$  and, as indicated in the legend, (a) impact of increasing the vertical wind shear, (b) selecting different  $u$  does not reproduce the effect of vertical shear, and (c) the value of the fall speed can be tuned to closely match the effect of shear.

importance of the various parameters within a self-consistent framework. For the range of values considered (Tables 1 and 2) all the parameters can have a significant control on the precipitation pattern (Figs. 3 to 7). If the moisture scale height is low compared to the mountain height ( $\alpha = H/H_m \gg 1$ ), precipitation will maximize low on the windward flank (and precipitation efficiency will be high); if the moisture layer is deep, precipitation will occur nearer the crest. Evaporation is effective when its characteristic depth scale is small compared to mountain height ( $\xi = H/\tau_{ev}v_f \ll 1$ ), and

results in a strong rain shadow. If the mountain width is large compared to growth length scale for hydrometeors (i.e.,  $\psi_1 = L_1/u\tau_g \gg 1$ ), the maximum precipitation rate will occur along the windward flank. If it is small, precipitation efficiency is reduced. Indeed, there may be no precipitation at all if cloud particles are advected beyond the source region before reaching threshold size to fall. If the trajectory slopes are steep compared to the mountain slopes ( $\theta_1 = L_1v_f/uH \gg 1$ ), precipitation efficiency can be at, or exceed, 100%, and the maximum will be located down on the windward divide.

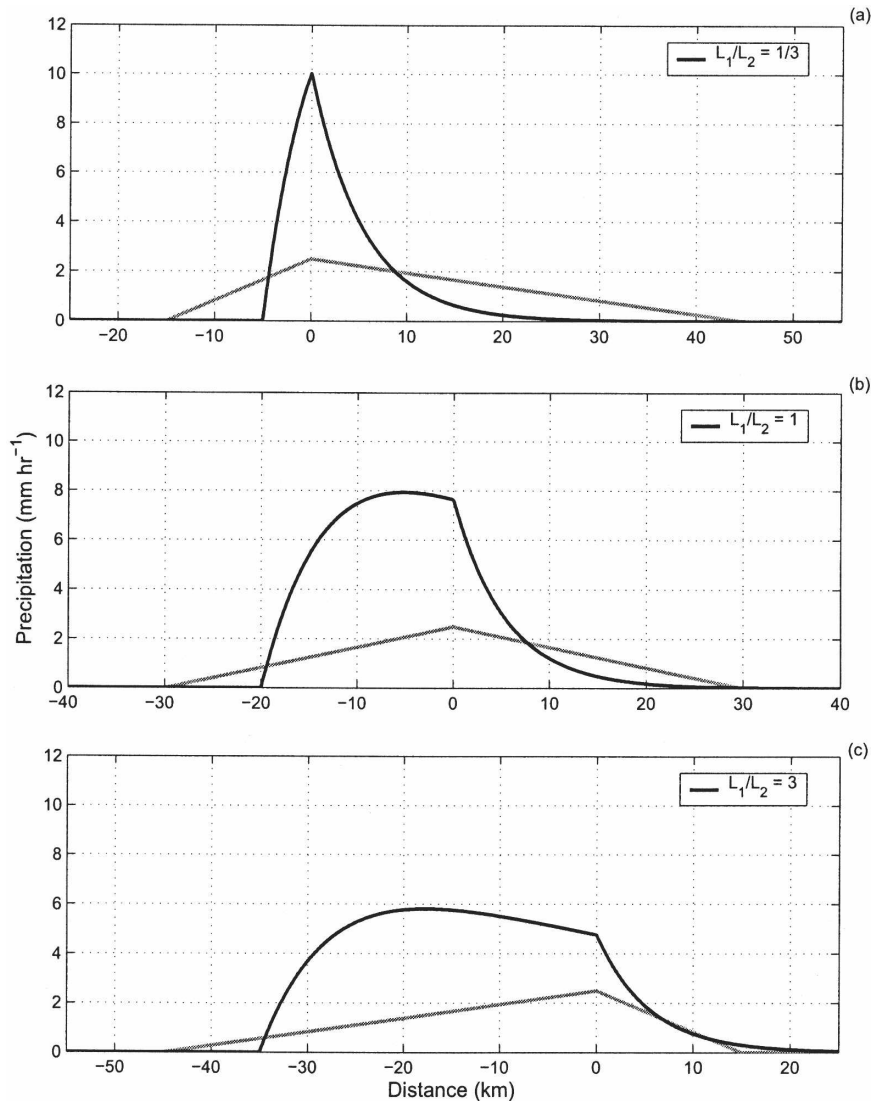


FIG. 10. Asymmetry of the mountain range. The ratio of  $L_1$  to  $L_2$  is varied (but with  $L_1 + L_2 = 60$  km). Otherwise the standard parameter set is used. The maximum precipitation rate and the strength of the rain shadow depend on the asymmetry and because of the finite formation time and evaporation time scale, so does the total precipitation rate.

Shallower trajectories reduce precipitation efficiency, push the maximum toward the divide, and produce significant leeward precipitation.

The sensitivity of the pattern to variations in these parameters means that even during a single storm the pattern of the orographic component of the precipitation must be expected to change. This can also be inferred from observations (e.g., Hobbs et al. 1980; Herzegh and Hobbs 1980; Yuter and Houze 2003; Yuter et al. 2004, manuscript submitted to *J. Atmos. Sci.*; A04), and mesoscale models (e.g., Lang and Barros 2002; Smith et al. 2003; A04; Colle 2004). Therefore, even for a single storm and certainly on a climatological

basis, model parameters must be regarded as characteristic or effective values incorporating the integrated effects of some complicated interactions, rather than reflecting actual physical values.

There are two main conceptual categories of simplified models of orographic precipitation. One focuses on the seeder–feeder mechanism in which washout of droplets (or ice) from the orographic cloud occurs through accretion onto preexisting hydrometeors (e.g., Bader and Roach 1977; Carruthers and Choullarton 1983; Choullarton and Perry 1986; Robichaud and Austin 1988). The others, like ours, (upslope models), concentrate on the rate of condensation during the ascent

of air and then distribute that as precipitation over the surface according to parameterization of microphysics schemes, or with some more arbitrary downwind smoothing of the condensation patterns (e.g., Sawyer 1956; Alpert 1986; Roe 2002; Smith and Barstad 2004). To a certain extent the distinction between these approaches is blurred and somewhat artificial. The common theme of these models is that ascent on a windward flank produces a condensation region (i.e., our source region). How (and if) that condensation reaches the ground as precipitation depends on the dominant conversion mechanisms operating at the time. Selection of the right parameters can emulate these different mechanisms. For example, in the seeder–feeder process, condensate is immediately incorporated into hydrometeors through accretion. Our model and those of, for example, Sinclair (1994) and Smith and Barstad (2004) are able to represent this by a short growth time,  $\tau_g$ .

There are, though, some potentially important differences in formulation of these models. For example, most simple upslope models integrate the condensation rate in a vertical column. In actuality, the slanting of hydrometeor trajectories means that precipitation arriving at a surface point did not all originate from the same horizontal distance upwind. Some aspects of the precipitation pattern might allow for some discrimination between models. The finite formation time in our model creates a maximum precipitation rate at intermediate horizontal wind speed: although the condensation rate increases with wind strength, the width of the source region decreases. At some point, as the winds increase, this latter effect comes to dominate, and precipitation decreases. This effect is present in the nonlinear treatment of Jiang and Smith (2003), but does not occur in a seeder–feeder model or in typical upslope formulations (e.g., Alpert 1986; Sinclair 1994) in which precipitation increases linearly with wind strength. Secondly, with strong enough winds (or low enough fall speeds), our model can give rise to a reverse rain shadow with more precipitation falling leeward than windward (Fig. 7). Last, our model also leads to apparent localized precipitation efficiencies well in excess of 100%, again due to the finite formation time and slanting hydrometeor trajectories. Ascertaining whether any of these effects are seen in a dense network of rain-gauge data, or under controlled conditions in mesoscale models would be an important test. A confounding factor in this type of analysis is that, in reality, model parameters are not necessarily independent. If, for example, as  $u$  increases, the precipitation changes from stratiform to convective, the appropriate value of  $\tau_g$  likely changes, in turn affecting the pattern.

Smith and Barstad (2004) present a highly adaptable orographic precipitation model incorporating a linear atmospheric response and capable of efficient calculation over complex terrain. In the configuration analogous to ours (triangular ridge, dynamics switched off) their precipitation always maximizes on, or leeward of, the crest (unlike our model), and precipitation rates diminish much more slowly as  $u$  increases. In their approach, condensation in the source region is integrated in a vertical column and redistributed as surface precipitation exponentially by a characteristic conversion time scale and a characteristic fallout time scale. By contrast, this redistribution occurs in our model because of a finite growth time and slanting hydrometeor trajectories. In these two approaches then, precipitation has arrived at the surface from different regions within the source region, and this gives rise to the differences noted above. It remains to be seen, however, whether this effect can practically be discerned in observations. A clear way forward would be to compare these simpler models with a mesoscale model akin to that of Colle (2004) and to identify where the precipitation arriving at the ground originated, and to evaluate the relative importance of the different causes of the pattern.

The analytical solution presented was obtainable only for a simplified mountain geometry. In reality, parcels undergo multiple ascents and descents over individual ridges and valleys and can become well mixed during their journey. Among other things this makes the physical meaning of a local measure like precipitation efficiency unclear (Smith et al. 2003). The assumed flow response in our model is also unrealistic but it enabled us to specify a uniform windward source region. The details of the atmospheric response can in some cases importantly modify the shape and strength of the source region and hence also the pattern of precipitation (e.g., Smith 1979; Robichaud and Austin 1988; Smith and Barstad 2004; Colle 2004). Furthermore, the model has also omitted many other processes that have been shown to be important in orographic precipitation: blocking (e.g., Katzfey 1995a,b; Rotunno and Ferretti 2001), modification of the atmospheric flow by latent heating (e.g., Jiang 2003), orographic triggering of convective instability (e.g., Medina and Houze 2003), evaporative cooling (Barros and Lettenmeier 1994b), valley circulations (Steiner et al. 2003), and multiphase clouds (e.g., Yuter and Houze 2003). This latter situation can be incorporated in a version of our model with two layers, each with different growth times, wind speeds, and fall velocities; the freezing level then becomes another parameter in the model [Colle (2004) also considers the effect of the freezing level]. Even in situations where these other mechanisms ap-

ply, the model results for the relative importance of formation time, advection time, and evaporation as a function of mountain scale, for example, are likely to still have meaning. It also remains to be asked whether these other mechanisms are important in setting the climatological patterns of precipitation or if the sensitivity to changes in forcing can be qualitatively understood in terms of a modified upslope model such as that of Smith and Barstad (2004) or the one presented here.

The results of this and other studies show that even greatly simplified representations of orographic precipitation contain a rich and interesting set of possibilities, the investigation of which is a step toward a greater understanding of the controls on what is one of the most important interactions between the land surface and the atmosphere.

*Acknowledgments.* The authors are grateful to Ron Smith, Socorro Medina, Dale Durran, and Sandra Yuter for insightful and instructive conversations. And to Matthias Steiner and two anonymous reviewers for thoughtful and constructive reviews which improved the manuscript, and to George Craig, the editor. MBB acknowledges support from NSF Grant ATM 02-11247.

APPENDIX A

**Analytical Expressions for Windward and Leeward Precipitation Totals**

*a. Source line equations*

We here develop the equations for the source lines using Fig. 1. There are three source line functions to consider: one for  $x_s < 0$ , one for  $0 < x_s < L_2$ , and one for  $x_s > L_2$ . First, for condensation occurring at  $(x, z)$  the point  $A_{II}$  can be expressed as  $(x + u\tau_g, z + w_1\tau_g)$ . Then, from its geometry, the line  $A_{II}$ - $A_{III}$  must satisfy the relation

$$\frac{(z + w_1\tau_g) - z_s}{x_s - (x + u\tau_g)} = \frac{v_f - w_1}{u}, \tag{A1}$$

which on substituting  $w_1 = uH/L_1$  and rearranging gives

$$z + \frac{v_f}{u} \left( 1 - \frac{uH}{v_f L_1} \right) x = z_s + \frac{v_f}{u} \left( 1 - \frac{uH}{v_f L_1} \right) x_s - v_f \tau_g. \tag{A2}$$

Equation (A2) gives the source line for any windward  $(x_s, z_s)$ .

Next, for the source line for the region to the lee of the crest  $0 \leq x_s < L_2$ . Again from the geometry of the trajectories

$$\begin{aligned} B_{II}-B_{III}: \frac{(z + w_1\tau_g) - z_0}{0 - (x + u\tau_g)} &= \frac{v_f - w_1}{u} = \frac{v_f}{u} \left( 1 - \frac{uH}{v_f L_1} \right) \\ B_{III}-B_{IV}: \frac{z_0 - z_s}{x_s - 0} &= \frac{v_f + w_2}{u} = \frac{v_f}{u} \left( 1 + \frac{uH}{v_f L_2} \right), \end{aligned} \tag{A3}$$

where  $z_0$  is the altitude of the trajectory at  $x = 0$ . Eliminating  $z_0$  and rearranging gives

$$z + \frac{v_f}{u} \left( 1 - \frac{uH}{v_f L_1} \right) x = z_s + \frac{v_f}{u} \left( 1 + \frac{uH}{v_f L_2} \right) x_s - \tau_g v_f. \tag{A4}$$

Last, for  $x_s > L_2$ , the last portion of the raindrop trajectory is through air with no vertical velocity

$$\begin{aligned} C_{II}-C_{III}: \frac{(z + w_1\tau_g) - z_0}{0 - (x + u\tau_g)} &= \frac{v_f - w_1}{u} = \frac{v_f}{u} \left( 1 - \frac{uH}{v_f L_1} \right) \\ C_{III}-C_{IV}: \frac{z_0 - z_{L_2}}{L_2 - 0} &= \frac{v_f + w_2}{u} = \frac{v_f}{u} \left( 1 + \frac{uH}{v_f L_2} \right) \\ C_{IV}-C_V: \frac{z_{L_2} - 0}{x_s - L_2} &= \frac{v_f}{u}, \end{aligned} \tag{A5}$$

where  $z_{L_2}$  is the altitude of the raindrop trajectory at  $x = L_2$ . Eliminating  $z_0$  and  $z_{L_2}$  gives

$$z + \frac{v_f}{u} \left( 1 - \frac{uH}{v_f L_1} \right) x = H + \frac{x_s v_f}{u} - v_f \tau_g. \tag{A6}$$

Equations (A6) and (A4) are in, fact, the same, which can be seen by substitution of Eq. (1). Equations (A2) and (A6) therefore give source lines, locations of sources of precipitation which will fall at  $(x_s, z_s)$ .

*b. Calculations of  $z_{\max}$  and  $z_{\min}$*

Using these source lines we can calculate the  $z_{\min}$  and  $z_{\max}$  for (5a)–(5c). From Fig. 1, the windward  $z_{\min}$  comes from the intersection of the source line [i.e., (A2)] and the topography. That is,  $z_{\min} = z$ , where  $z = (H/L_1)(L_1 + x)$ , which gives

$$\begin{aligned} z_{\min} \left( \frac{L_1 v_f}{uH} \right) &= z_s + \frac{v_f}{u} x_s \left( 1 - \frac{uH}{v_f L_1} \right) - v_f \tau_g \\ &+ \frac{L_1 v_f}{u} \left( 1 - \frac{uH}{v_f L_1} \right), \end{aligned} \tag{A7}$$

which on substitution from Eq. (1) simplifies to

$$z_{\min} = z_s - \frac{u\tau_g H}{L_1}; \tag{A8}$$

$z_{\max}$  is given by (A2), where  $z_{\max} = z$  and  $x = -L_1$

$$z_{\max} = z_s + \frac{v_f}{u} x_s \left(1 - \frac{uH}{v_f L_1}\right) - v_f \tau_g + \frac{L_1 v_f}{u} \left(1 - \frac{uH}{v_f L_1}\right); \quad (\text{A9})$$

hence,

$$z_{\max} = \frac{L_1 v_f}{uH} z_{\min}. \quad (\text{A10})$$

For the leeward flank it has already been noted that there is a single source line equation. Starting with Eq. (A6),  $z_{\min} = z$ , where  $x = -u\tau_g$ , and  $z_{\max} = z$ , where  $x = -L_1$

$$z_{\min} = H + \frac{x_s v_f}{u} - \frac{\tau_g u H}{L_1}. \quad (\text{A11})$$

From the geometry of the source line,  $z_{\max}$  can be obtained,

$$\frac{z_{\max} - z_{\min}}{-u\tau_g - (-L_1)} = \frac{v_f - w_1}{u} = \frac{v_f}{u} \left(1 - \frac{uH}{v_f L_1}\right), \quad (\text{A12})$$

which on rearranging yields

$$z_{\max} = z_{\min} + (L_1 - u\tau_g) \frac{v_f}{u} \left(1 - \frac{uH}{v_f L_1}\right). \quad (\text{A13})$$

These expressions can be substituted into Eq. (5) to give the precipitation rate.

### c. Windward and leeward precipitation totals

Using Eqs. (9) and (10), expressions can also be obtained for the integrated windward and leeward precipitation totals

$$P_W = \int_{-L_1 + u\tau_g}^0 R(x_s) dx_s, \quad (\text{A14})$$

which on substitution from (9) and tidying up gives

$$P_W = \left(\frac{\theta_1}{\theta_1 - 1}\right) \frac{R_0 L_1}{\alpha} \left\{1 - \exp\left[-\alpha\left(1 - \frac{1}{\psi_1}\right)\right] - \frac{1}{\theta_1} + \frac{1}{\theta_1} \exp\left[-\alpha\theta_1\left(1 - \frac{1}{\psi_1}\right)\right]\right\}. \quad (\text{A15})$$

For the leeward flank

$$P_L = \int_0^{L_2} R(x_s) dx_s, \quad (\text{A16})$$

which using (10) produces

$$P_L = \left(\frac{\theta_1}{\theta_1 - 1}\right) \frac{R_0 L_2}{\theta_2(\xi + \alpha)} \times \left\{1 - \exp\left[-\alpha\left(1 - \frac{1}{\psi_1}\right)(\theta_1 - 1)\right]\right\} \times \exp\left[-\alpha\left(1 - \frac{1}{\psi_1}\right)\right] (1 - \exp[-\theta_2(\xi + \alpha)]). \quad (\text{A-17})$$

The strength of the rain shadow can be defined as  $P_W/P_L$ .

## APPENDIX B

### Microphysical Parameters

Here we provide approximations to the microphysical equations that allow us to estimate values of the following parameters:  $\tau_g$ ,  $v_f$ ,  $\tau_{\text{evap}}$ , and  $\tau_{\text{moist}}$ —the time scale for moistening the leeward air due to hydrometeor evaporation into it. Note that, if the radii of the hydrometeors in the cloud approaching the mountain are already above their threshold values at  $x = -L_1$ , they will produce precipitation with no preliminary growth period. Since we are concerned here with orographic enhancement of precipitation, we ignore this contribution to the precipitation pattern.

We assume two growth mechanisms: vapor deposition and collection of cloud particles. Thus we neglect interactions among falling hydrometeors. The mass of a cloud drop of radius  $r$  at altitude  $z$  changes in time according to the equation

$$\frac{dm}{dt}(r, z) = \frac{dm}{dt}\Big|_v(r, z) + \frac{dm}{dt}\Big|_{\text{coll}}(r, z). \quad (\text{B1})$$

### a. Vapor deposition

For a single hydrometeor

$$\frac{dm}{dt}\Big|_v(r, z) = rG\rho q_s(z)[\sigma(z) - 1] \quad (\text{B2})$$

where  $G \sim 10^{-5} \text{ m}^2 \text{ s}^{-1}$  is a slowly varying function of temperature  $T(z)$ ;  $\sigma(z)$  is the supersaturation (relative to ice or water) in the cloud.

In the case of liquid drops growing in a warm cloud and ice crystals growing in a fully glaciated one, we assume that the depositional growth rate just balances the rate of liberation of vapor in the rising air so that Eq. (B2) can be replaced by

$$\left. \frac{dm}{dt} \right|_v (r, z) = \frac{\alpha w \rho q_0 \exp(-\alpha z)}{n} \quad (\text{B3})$$

where  $n$  ( $\text{m}^{-3}$ ) is the droplet (or ice particle) number density.

*b. Growth via collection*

$$\left. \frac{dm}{dt} \right|_{\text{coll}} (r, z) = \pi r^2 E v_j(r) \rho_{\text{cloud}}, \quad (\text{B4})$$

where  $E$  is the collision–collection efficiency, assumed constant, and  $\rho_{\text{cloud}}$  ( $\text{kg m}^{-3}$ ) is the density of the cloud condensate (water or ice).

*c. Fall velocities of hydrometeors*

We use the fits to fall velocity  $v_f(r)$  from Johnston (1982) for raindrops and from Hobbs et al. (1973) for rimed crystals and graupel. We also use the Hobbs et al. parameterized relationships linking the effective radii of ice and graupel particles to their masses.

*d. Evaporation of hydrometeors*

Evaporation rates are computed from Eq. (B2), substituting the relative humidity (RH) with respect to water or ice (assumed constant in the leeward air) for the saturation  $\sigma(z)$ .

1) PRECIPITATION PARTICLE TYPES

Using the simple approach outlined here we have simulated trajectories of liquid drops, graupel particles, and rimed ice crystals through orographic clouds. The lightly rimed ice crystals falling through ice clouds and the drops falling through liquid clouds represent two extreme cases; we therefore use parameters derived from these two extreme cases to guide our parameter choices (Tables 1 and 2).

2) RESULTS

We assume condensate density is zero at  $x = -L_1$ ,  $z = 0$  and that it rises adiabatically with height. It does not vary with time. This means we neglect

- 1) variation of the phase of the condensate in time and/or space;
- 2) the existence of a subcloud layer;
- 3) depletion of the cloud by precipitation.

Furthermore, we assume

- 1)  $E = 1$  for the drops,  $E = 0.5$  for the ice crystals.
- 2)  $T(z = 0) = 273.15$  for the ice cloud,  $T(z = 0) = 288$  K for the liquid cloud.
- 3) RH = 95% on the lee side of the mountain.

- 4) Standard mountain case (Table 1).
- 5) Initial radii  $10 \leq r(0) \leq 200 \mu\text{m}$ .
- 6)  $10^6 \leq n \leq 10^8 \text{ m}^{-3}$ .
- 7) Particle growth beginning at a range of altitudes  $2 \leq z_i \leq 6$  km and a range of horizontal locations  $-30 \leq x_i \leq -10$  km.

Figure B1 shows sample trajectories for raindrops growing from drops of initial radii  $10 \mu\text{m}$  at  $z_i = 2$  km and various values of  $x_i$ , falling through a liquid cloud, and for ice particles with the same starting conditions growing in a fully glaciated cloud. The cloud droplet number for these simulations was  $10^6 \text{ m}^{-3}$  and the cloud ice particle slightly lower. For these parameters there is no windward precipitation in the ice case.

- $\tau_g$ : In our standard mountain case  $w = 0.83 \text{ m s}^{-1}$ ; this is the fall velocity of a droplet of radius  $\sim 135 \mu\text{m}$ , a graupel particle of linear dimension  $\sim 450 \mu\text{m}$ , and a lightly rimed ice crystal of approximately 1 mm. We define  $\tau_g$  to be the time it takes for a hydrometeor to grow to this size starting from  $r = 10 \mu\text{m}$ . In the simulations  $\tau_g$  ranged from 600 to about 1000 s for the drops, 3000–6000 s for the ice crystals. This value depends on the droplet or cloud ice particle number density [see Eq. (B3)] and the location where the small particles form.
- $v_f$ : The terminal velocities increase as the particles fall. The rate of increase is roughly proportional to  $\rho_{\text{cloud}}$ , the cloud condensate, and therefore to some extent on position in the cloud where the fall begins. In our simulations fall velocities increase throughout the descent, reaching maximum values of about  $4 \text{ m s}^{-1}$  for the drops and  $2 \text{ m s}^{-1}$  for the ice crystals on the windward side of the mountain.
- $\tau_{\text{evap}}$ : The evaporation time scale for a hydrometeor exiting the cloud with radius  $r(z_0)$  at altitude  $z_0$  varies approximately as  $r^2(z_0)$ . This parameter is the most variable over the ranges of input parameters we tried, evaporation times varied from 100 to 12 000 s, depending on where the particles formed and type of particle.

3) MOISTENING RATE

The total amount of liquid water condensed on the windward side of the mountain is  $C$  [ $\text{kg m}^{-1} \text{ s}^{-1}$ ] =  $\rho q_0 u H_m [1 - \exp(-H/H_m)] = R_0 L_1 / \alpha [1 - \exp(-\alpha)]$ . The total amount of precipitation hitting the ground on the windward (leeward) side is  $P_w$  ( $P_L$ ) [ $\text{kg m}^{-1} \text{ s}^{-1}$ ] (see appendix A), so the total rate of moistening of the leeward air is  $\dot{M}$  [ $\text{kg m}^{-1} \text{ s}^{-1}$ ] =  $C - (P_w + P_L)$ .

The moisture deficit in the leeward air ( $0 \leq x_s$ ) is  $\Delta M$  [ $\text{kg m}^{-1}$ ] =  $\rho(1 - \text{RH})q_0 H_m L_2 [1 - \exp(-H/H_m)]$  as-

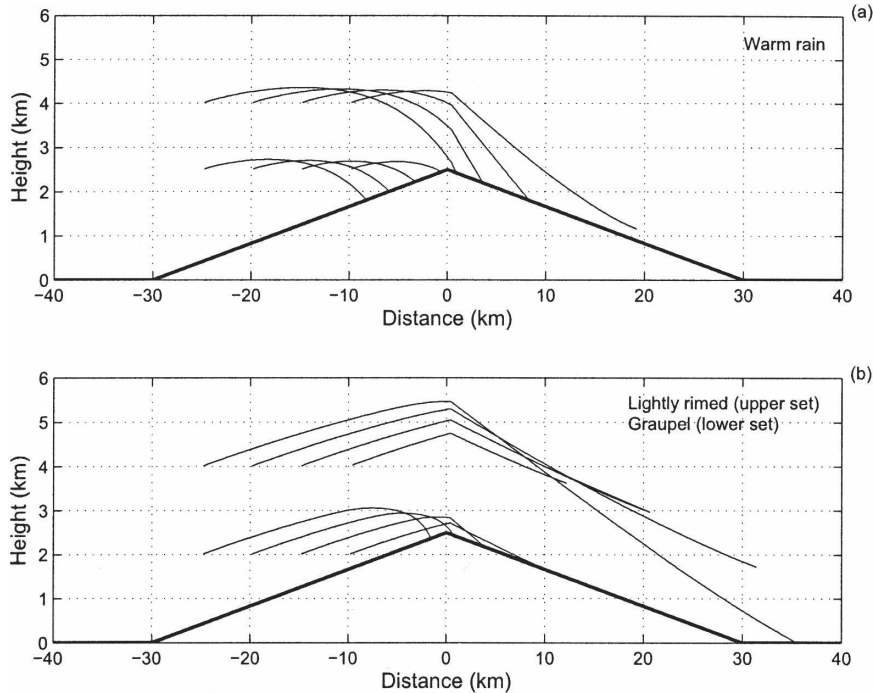


FIG. B1. Calculated trajectories from microphysical calculations in appendix B, beginning from an initial drop radius of  $10\ \mu\text{m}$  and cloud droplet number  $10^6\ \text{m}^{-3}$ . (a) Sample trajectories for rain (both sets), (b) sample trajectories for lightly rimed particles (upper set) and graupel (lower set). These trajectories are approximated by the straight lines in Fig. 1.

suming constant relative humidity throughout the column, and the time constant for moistening the layer is therefore  $\tau_M \sim (\Delta M/\dot{M})$ ;  $\tau_M \leq 1\ \text{h}$  over the entire range of conditions simulated here.

### APPENDIX C

#### Trajectories Including Vertical Wind Shear

The effect of vertical wind shear can be incorporated into the model by calculating the appropriate shape of the source lines, and inserting the values of  $z_{\min}$  and  $z_{\max}$  into Eqs. (9) and (10). When wind shear is included raindrops follow parabolic trajectories [illustrated in Fig. (8)]. Although not necessary, it is simpler to calculate the source lines assuming zero growth time (i.e.,  $\tau_g = 0$ ): conversion to hydrometeors occurs as soon as condensation occurs.

Let the wind be described by

$$u = u_0 + u_z \times z, \quad (\text{C1})$$

where  $u_z$  is the vertical shear (assumed constant). As in section 2, we calculate the source line equation for a point on the surface  $x_s$ . Let the hydrometeor start falling from height  $z = z_i$  at  $t = 0$ . If  $x_s > 0$ , let  $z_0$  be its

height when its trajectory crosses  $x = 0$  at time  $t = t_0$ . The height of this hydrometeor as a function of time is

$$\begin{aligned} z &= z_i - (v_f - w)t, & -L_1 < x \leq 0 \\ z &= z_0 - (v_f + w)(t - t_0), & 0 \leq x. \end{aligned} \quad (\text{C2})$$

Substituting these expressions into (C1) and integrating gives horizontal position as a function of time. For  $x_s < 0$ , integrating between  $x_i$  at  $t = 0$  and  $x_s$  at time  $t$  and rearranging gives an equation for the source line for the point  $x_s$  as a function of  $(x_i, z_i)$

$$x_s - x_i = (u_0 + u_z z_i)t - u_z(v_f - w)\frac{t^2}{2} \quad (\text{C3})$$

where

$$t = \frac{z_i - z_s}{(v_f - w)}.$$

For  $x_s \leq 0$ ,  $z_{\min} = z_s$  and  $z_{\max}$  can be calculated by solving the above quadratic equation for  $x_i = -L_1$  (only one root is meaningful).

For  $0 < x_s \leq L_2$ ,  $z_{\min} = z_0$  and  $z_0$  is determined from a similar equation,

$$x - L_2 = (u_0 + u_z z_0)(t - t_0) - u_z(v_f + w)\frac{(t - t_0)^2}{2},$$

where

$$t - t_0 \equiv \frac{z_0 - z_s}{(v_f + w)}. \quad (C4)$$

The above expressions can be framed in nondimensional terms by introducing the parameter  $\lambda = Hu_z/u$ :

$$\frac{\lambda}{2} \left( \frac{z_{\max}}{H} \right)^2 + \left( \frac{z_{\max}}{H} \right) - \frac{\lambda}{2} \left( \frac{z_{\min}}{H} \right)^2 - \left( \frac{z_{\min}}{H} \right) - (\theta_1 - 1) \left( \frac{x_s}{L_1} + 1 \right) = 0. \quad (C5)$$

For  $x_s \leq 0$   $z_{\min} = z_s$  and for  $0 < x_s \leq L_2$   $z_{\min} = z_0$ , where  $z_0$  is the solution to

$$\frac{\lambda}{2} \left( \frac{z_0}{H} \right)^2 + \left( \frac{z_0}{H} \right) - \frac{\lambda}{2} \left( \frac{z_s}{H} \right)^2 - \left( \frac{z_s}{H} \right) - (\theta_2 + 1) \left( \frac{x_s}{L_2} \right) = 0. \quad (C-6)$$

For  $x_s > L_2$ , where there is no vertical motion, the equivalent expression is

$$\frac{\lambda}{2} \left( \frac{z_0}{H} \right)^2 + \left( \frac{z_0}{H} \right) - \theta_2 \left( \frac{x_s}{L_2} \right) - 1 = 0. \quad (C-7)$$

These equations are used to determine the precipitation pattern in Fig. (9).

REFERENCES

Alpert, P., 1986: Mesoscale indexing of the distribution of orographic precipitation over high mountains. *J. Climate Appl. Meteor.*, **25**, 532–545.

Bader, M. J., and W. T. Roach, 1977: Orographic rainfall in warm sectors of depressions. *Quart. J. Roy. Meteor. Soc.*, **103**, 269–280.

Barros, A. P., and D. P. Lettenmaier, 1993: Dynamic modeling of the spatial distribution of precipitation in remote mountainous areas. *Mon. Wea. Rev.*, **121**, 1195–1214.

—, and —, 1994a: Dynamic modeling of orographically induced precipitation. *Rev. Geophys.*, **32**, 265–284.

—, and —, 1994b: Incorporation of an evaporative cooling scheme into a dynamic model of orographic precipitation. *Mon. Wea. Rev.*, **122**, 2777–2783.

Beaumont, C., P. Fullsack, and J. Hamilton, 1992: Erosional control of active compressional orogens. *Thrust Tectonics*, K. R. McClay, Ed., Chapman and Hall, 1–18.

Browning, K. A., F. F. Hill, and C. W. Pardoe, 1974: Structure and mechanism of precipitation and the effect of orography in a wintertime warm sector. *Quart. J. Roy. Meteor. Soc.*, **100**, 309–330.

Caine, N., 1980: The rainfall intensity: Duration controls on shallow landslides and debris flows. *Geogr. Ann. Series A*, **62**, 23–27.

Carruthers, D. J., and T. W. Choullarton, 1983: A model of the feeder-seeder mechanism of orographic rain including strati-

fication and wind-drift effects. *Quart. J. Roy. Meteor. Soc.*, **109**, 575–588.

Choullarton, T. W., and S. J. Perry, 1986: A model of the orographic enhancement mechanism of snowfall by the seeder-feeder mechanism. *Quart. J. Roy. Meteor. Soc.*, **112**, 335–345.

Colle, B. A., 2004: Sensitivity of orographic precipitation to changing ambient conditions and terrain geometries: An idealized modeling perspective. *J. Atmos. Sci.*, **61**, 588–606.

—, K. J. Westrick, and C. F. Mass, 1999: Evaluation of the MM5 and Eta-10 precipitation forecasts over the Pacific Northwest during the cool season. *Wea. Forecasting*, **14**, 137–154.

Colton, D. E., 1976: Numerical simulation of the orographically induced precipitation distribution for use in hydrologic analysis. *J. Appl. Meteor.*, **15**, 1241–1251.

Conway, H., and C. F. Raymond, 1993: Snow stability during rain. *J. Glaciol.*, **39**, 635–642.

Daly, C., R. P. Neilson, and D. L. Phillips, 1994: A statistical-topographic model for mapping climatological precipitation over mountainous terrain. *J. Appl. Meteor.*, **33**, 140–158.

Durrant, D. R., 1986: Mountain waves. *Mesoscale Meteorology and Forecasting*, P. Ray, Ed., Amer. Meteor. Soc., 472–492.

—, 2003: Lee waves and mountain waves. *The Encyclopedia of the Atmospheric Sciences*, J. Holton, J. Curry, and J. Pyle, Eds., Academic Press, 1161–1169.

Fraser, A. B., R. C. Easter, and P. V. Hobbs, 1973: A theoretical study of the flow of air and fallout of solid precipitation over mountainous terrain. Part I: Airflow model. *J. Atmos. Sci.*, **30**, 801–812.

Hobbs, P. V., R. C. Easter, and A. B. Fraser, 1973: A theoretical study of the flow of air and fallout of solid precipitation over mountainous terrain. Part II: Microphysics. *J. Atmos. Sci.*, **30**, 813–823.

—, T. J. Matejka, P. H. Herzegh, J. D. Locatelli, and R. A. Houze, 1980: The mesoscale and microscale structure and organization of clouds and precipitation in midlatitude cyclones. Part I: A case study of a cold front. *J. Atmos. Sci.*, **37**, 568–596.

Herzegh, P. H., and P. V. Hobbs, 1980: The mesoscale and microscale structure and organization of clouds and precipitation in midlatitude cyclones. Part II: Warm frontal clouds. *J. Atmos. Sci.*, **37**, 597–611.

Jiang, Q., 2003: Moist dynamics and orographic precipitation. *Tellus*, **55A**, 301–316.

—, and R. B. Smith, 2003: Cloud time scales and orographic precipitation. *J. Atmos. Sci.*, **60**, 1543–1558.

Johnson, D. B., 1982: The role of giant and ultragiant aerosol particles in warm rain initiation. *J. Atmos. Sci.*, **39**, 448–460.

Kageyama, M., P. J. Valdes, G. Ramstein, C. Hewitt, and U. Wypulla, 1999: Northern Hemisphere storm tracks in present day and Last Glacial Maximum climate simulations: A comparison of the European PMIP models. *J. Climate*, **12**, 742–760.

Katzfey, J. J., 1995a: Simulation of extreme New Zealand precipitation events. Part I: Sensitivity of orography and resolution. *Mon. Wea. Rev.*, **123**, 737–754.

—, 1995b: Simulation of extreme New Zealand precipitation events. Part II: Mechanisms of precipitation development. *Mon. Wea. Rev.*, **123**, 755–775.

Lang, J. T., and A. P. Barros, 2002: An investigation of the onsets of the 1999 and 2000 monsoons in central Nepal. *Mon. Wea. Rev.*, **130**, 1299–1316.

—, and —, 2004: Winter storms in the central Himalayas. *J. Meteor. Soc. Japan*, **82**, 829–844.

- Medina, S., and R. A. Houze Jr., 2003: Air motions and precipitation growth in alpine storms. *Quart. J. Roy. Meteor. Soc.*, **129**, 345–371.
- Montgomery, D. R., G. Balco, and S. D. Willett, 2001: Climatic, tectonics, and the morphology of the Andes. *Geology*, **29**, 579–582.
- Myers, V. A., 1962: Airflow on the windward side of a ridge. *J. Geophys. Res.*, **67**, 4267–4291.
- Nordø, J., and K. Hjortnæs, 1966: Statistical studies of precipitation on local, national, and continental scales. *Geofys. Publ.*, **26**, 1–46.
- Peixoto, J. P., and A. H. Oort, 1992. *Physics of Climate*. American Institute of Physics, 520 pp.
- Robichaud, A. J., and G. L. Austin, 1988: On the modeling of warm orographic rain by the seeder-feeder mechanism. *Quart. J. Roy. Meteor. Soc.*, **114**, 967–988.
- Reiners, P. W., T. A. Ehlers, S. G. Mitchell, and D. R. Montgomery, 2003: Coupled spatial variations in precipitation and long-term erosion rates across the Washington Cascades. *Nature*, **426**, 645–647.
- Rhea, J. O., 1978: Orographic precipitation model for hydro-meteorological use. Colorado State University Atmospheric Paper 287, 198 pp.
- Roe, G. H., 2002: Modeling precipitation over ice sheets: An assessment using Greenland. *J. Glaciol.*, **48**, 70–80.
- , and R. S. Lindzen, 2001: The mutual interaction between continental-scale ice sheets and atmospheric stationary waves. *J. Climate*, **14**, 1450–1465.
- Rotunno, R., and R. Ferretti, 2001: Mechanisms of intense alpine rainfall. *J. Atmos. Sci.*, **58**, 1732–1749.
- Sanberg, J. A. M., and J. Oerlemans, 1983: Modeling of Pleistocene European ice sheets: the effect of upslope precipitation. *Geol. Mijnbouw*, **62**, 267–273.
- Sarker, R. P., 1966: A dynamical model of orographic rainfall. *Mon. Wea. Rev.*, **94**, 555–572.
- Sawyer, J. S., 1956: The physical and dynamical problems of orographic rain. *Weather*, **11**, 375–381.
- Sinclair, M. R., 1994: A diagnostic model for estimating orographic precipitation. *J. Appl. Meteor.*, **33**, 1163–1175.
- Smith, R. B., 1979: The influence of mountains on the atmosphere. *Advances in Geophysics*, Vol. 21, Academic Press, 87–230.
- , 2003: A linear upslope time-delay model for orographic precipitation. *J. Hydrol.*, **282**, 2–9.
- , and I. Barstad, 2004: A linear theory of orographic precipitation. *J. Atmos. Sci.*, **61**, 1377–1399.
- , Q. Jiang, M. G. Fearon, R. Tabary, M. Dorninger, J. D. Doyle, and R. Benoit, 2003: Orographic precipitation and air mass transformation: An Alpine example. *Quart. J. Roy. Meteor. Soc.*, **129**, 433–454.
- Steiner, M., O. Bousquet, R. A. Houze, B. F. Smull, and M. Mancini, 2003: Airflow within major Alpine river valleys under heavy rainfall. *Quart. J. Roy. Meteor. Soc.*, **129**, 411–431.
- Willett, S. D., 1999: Orogeny and orography: The effects of erosion on the structure of mountain belts. *J. Geophys. Res.*, **104**, 28 957–28 981.
- Wratt, D. S., M. J. Revell, M. R. Sinclair, W. R. Gray, R. D. Henderson, and A. M. Chater, 2000: Relationships between air mass properties and mesoscale rainfall in New Zealand's Southern Alps. *Atmos. Res.*, **52**, 261–282.
- Yuter, S. E., and R. A. Houze, 2003: Microphysical modes of precipitation growth determined by S-band vertically pointing radar in orographic precipitation during MAP. *Quart. J. Roy. Meteor. Soc.*, **129**, 455–476.